Chemical Science

ROYAL SOCIETY OF CHEMISTRY

EDGE ARTICLE

View Article Online
View Journal | View Issue

Cite this: *Chem. Sci.*, 2025, **16**, 425

All publication charges for this article have been paid for by the Royal Society of Chemistry

Received 4th October 2024
Accepted 22nd November 2024

DOI: 10.1039/d4sc06727d

rsc.li/chemical-science

Buckled-layer $K_{1.39}Mn_3O_6$: a novel cathode for potassium-ion batteries†

Ang Li,[ab] Ziqi Wang[c] and Yunhua Xu *[a]

A novel buckled-layer $K_{1.39}Mn_3O_6$ cathode was synthesized, featuring P2-oxygen stacking and P3-K sites. The presence of two independent manganese sites significantly influences the charge distribution and diffusion pathways of potassium ions during the charge and discharge processes, resulting in exceptional electrochemical performance. A reversible capacity of 105 mA h g^{-1} at 100 mA g^{-1} and remarkable rate capability of 70 mA h g^{-1} at 1 A g^{-1} were achieved, surpassing those of most previously reported layered transition metal oxide cathodes. The findings facilitate the development of innovative cathode materials.

Introduction

Potassium-ion batteries (KIBs) are emerging as one of the most promising energy storage systems, owing to their abundant raw materials and the low redox potential of potassium.[1–7] Currently, potassium storage is primarily limited by the performance of cathodes. Significant efforts have been dedicated to the development and optimization of these cathodes.[8,9] Among the various candidates, layered transition metal oxides (K_xMO_2: $0 < x \leq 1$; M = Mn, Co, Cr, *etc.*) have garnered considerable attention due to their high theoretical capacity and cost-effectiveness.[10,11] However, they still face challenges, including sluggish thermodynamic kinetics and significant volume changes caused by the large K^+ radius (1.38 Å).

To address these challenges, modulating K^+ content or employing cationic/anion doping has proven to be an effective strategy.[12–14] Xiao *et al.* reported that a high K^+ content in K_x-$Mn_{0.7}Ni_{0.3}O_2$ enhances interlayer K^+–K^+ electrostatic repulsion, thereby reducing the energy difference between K^+ sites.[15] Lin *et al.* demonstrated that birnessite nanosheet arrays with high K content ($K_{0.77}MnO_2 \cdot 0.23H_2O$) exhibit ultrahigh reversible specific capacity.[12] Chen *et al.* found that the [Mn–Cu–Mg]O_6 octahedra in $K_{0.5}Mn_{0.8}Cu_{0.1}Mg_{0.1}O_2$ can reduce Mn^{3+} content and inhibit the Jahn–Teller effect by decreasing the redox activity of the Mn^{3+}/Mn^{4+} couple, thereby improving the cycling stability of the layered transition metal oxide cathode.[16] However, most of these results primarily focus on composition design, with limited attention given to structural modifications.

It is well known that the coordination environment of cathodes affects the charge distribution and diffusion path of K ions during the charge/discharge processes. The interior structure design of the MO_6 octahedra in K_xMO_2 can enhance electrochemical performance. Recently, a P2/P3 biphasic layered oxide composite was reported for potassium-ion batteries, benefiting from the high energy density of the P3 phase and the long cycle life of the P2 phase.[17] In the P2 phase, the mirror-symmetric structure (ABBA) of oxygen stacking allows K^+ ions to pass directly through two adjacent prismatic sites, resulting in excellent cycle stability. In contrast to the two different types of K sites (K_e and K_f) in the P2 phase, the K sites in the P3 phase are crystallographically equivalent, with edge-sharing interactions with MnO_6 octahedra on one side and face-sharing interactions on the other. The P3 phase, exhibiting reduced coulomb repulsion, possesses a higher reversible capacity. Therefore, the combination of P2-type oxygen stacking and P3-type K sites in the layered oxide cathode facilitates improved electrochemical performance.

Herein, buckled-layer $K_{1.39}Mn_3O_6$ (BL-KMO) was synthesized under the high pressure generated from the thermal decomposition of the MOF precursor (Fig. 1). The different

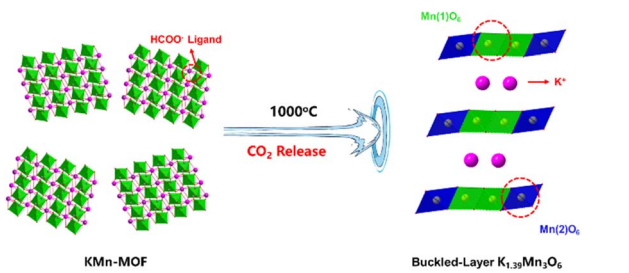

Fig. 1 Schematic illustration of the synthesis of buckled-layer $K_{1.39}Mn_3O_6$.

[a]*School of Materials Science and Engineering, Key Laboratory of Advanced Ceramics and Machining Technology (Ministry of Education), Tianjin Key Laboratory of Composite and Functional Materials, Tianjin University, Tianjin 300072, China. E-mail: yunhua.xu@tju.edu.cn*

[b]*School of Sciences, Civil Aviation University of China, Jinbei Road 2898, Tianjin 300300, Dongli District, P.R. China*

[c]*Aeronautical Engineering Institute, Civil Aviation University of China, Jinbei Road 2898, Tianjin 300300, Dongli District, P.R. China*

† Electronic supplementary information (ESI) available. See DOI: https://doi.org/10.1039/d4sc06727d

coordination environments of the edge-sharing $Mn(1)O_6$ and $Mn(2)O_6$ octahedra in the BL-KMO cathode result in two independent Mn sites with distinct octahedral environments. As a result, BL-KMO demonstrates excellent electrochemical performance, with a highly reversible capacity of 105 mA h g^{-1} at 100 mA g^{-1} and remarkable rate capability of 70 mA h g^{-1} at 1 A g^{-1}, surpassing those of most previously reported KMO cathodes (Table S1†). These findings facilitate the development of innovative cathode materials.

Experimental

Materials

Manganese(II) chloride tetrahydrate ($MnCl_2 \cdot 4H_2O$), potassium formate (HCOOK), formic acid (HCOOH), and methanol (CH_3OH) were all purchased from commercial suppliers—Aladdin for the manganese compound, Acros for potassium formate, and Tianjin Jiangtian Chemical Technology Co., Ltd for both formic acid and methanol—and were used as received without additional purification.

Synthesis of K[Mn(HCOO)$_3$]. The $K[Mn(HCOO)_3]$ precursor was prepared according to a previous report.[18] A mixture was prepared by combining 25 mL of a 25 mM solution of $MnCl_2 \cdot 4H_2O$ in methanol, 25 mL of a 20 mM solution of HCOOK in methanol, and 5 mL of formic acid in a 100 mL glass vial. The solution was then allowed to stand undisturbed at room temperature for a period of 24 hours. After this time, crystals formed and were subsequently collected, washed with methanol, and air-dried.

Synthesis of BL-KMO. The $K[Mn(HCOO)_3]$ precursor was loaded in a crucible and calcined in a tube furnace that was calcined at 1000 °C for 10 min with a heating rate of 10 °C in air. When it was cooled to 200 °C, the resulting product was immediately transferred and stored in a glove box with Ar.

Material characterization

X-ray diffraction (XRD) data was acquired using a Rigaku MiniFlex 600 diffractometer operated at 20 kV and 5 mA with a copper target X-ray tube. The morphology of the sample was analysed using a JEOL JSM-7500F scanning electron microscope (SEM). High-resolution transmission electron microscopy (HRTEM), conducted on a JEOL JEM F200 instrument, was employed to probe the structure of the sample. X-ray photoelectron spectroscopy (XPS) measurement was conducted with a PHI5000 Versaprobe system. Thermogravimetric analysis (TGA) was carried out on a Rigaku TG-DTA 8121 analyser, with the sample being heated from 25 to 900 °C at a rate of 10 °C min^{-1} in air.

Electrochemical tests

The preparation of the working electrodes involved spreading a mixture of BL-KMO, Ketjen black and polyvinylidene fluoride in a 7 : 2 : 1 weight ratio onto aluminum foil. CR2025 coin cells were fabricated using potassium foil as the counter electrode, 2.5 M potassium bis(fluorosulfonyl)imide triethyl phosphate as the electrolyte, and a glass fiber membrane as the separator in a glove box filled with highly pure argon gas (O_2 and H_2O: <0.1 ppm). Galvanostatic discharge/charge tests were performed in a voltage range of 2.0–4.2 V (*vs.* K/K^+) on Neware battery testing equipment. Cyclic voltammetry (CV) measurements were conducted with a Solartron 1470 Electrochemical Interface. Electrochemical impedance spectroscopy (EIS) was conducted using a Princeton VersaSTAT 4 workstation over a frequency range of 10^5–10^{-2} Hz with an AC amplitude of 5 mV.

Results and discussion

The KMn-MOF precursor was synthesized through a self-assembly process using manganese chloride tetrahydrate ($MnCl_2 \cdot 4H_2O$), potassium formate (HCOOK), and formic acid (HCOOH).[18] The structure of KMn-MOF was characterized as a highly distorted perovskite anionic framework, featuring MnO_6 octahedra interconnected by formate bridges, with K ions located in the channels (Fig. S1†). The XRD pattern of the as-synthesized KMn-MOF matches well with the simulated data, indicating successful synthesis (Fig. S2†). The test conditions for TGA reflect the pyrolysis process of MOFs during the preparation of BL-KMO. As depicted in Fig. S3,† a significant weight loss of 42.0% was observed between 250 and 410 °C, attributed to the decomposition of KM-MOF and the subsequent formation of metal oxides. Theoretically, the organic components should combust into CO_2, resulting in a weight loss of 57.6% according to theoretical calculations. Meanwhile, the formation of metal oxides is expected to account for a 14.0% weight gain due to the uptake of oxygen. The TGA results align well with these theoretical values. Additionally, a minor weight loss of 3.0% between 700 and 800 °C is indicative of potassium sublimation, likely due to its low boiling point of 759 °C. Significant amounts of CO_2 were released during this process, resulting in a high pressure. This may lead to structural changes in the MOF derivatives. Similar phenomena have been reported in the literature.[19]

Previous reports indicate that layered K_xMO_2 can be rapidly synthesized by heating KMn-MOF in a preheated tube furnace at 1000 °C for 8 minutes.[20] Taking into account the crystallinity of the MOF-derived K_xMO_2 and its structural rearrangement, the synthesis procedure for the derivatives in this work has been improved to include calcination at 1000 °C for 10 minutes with a heating rate of 10 °C min^{-1} in air. The buckled-layer crystal structure was revealed by the XRD pattern (Fig. 2a), which aligns well with previously reported results in the literature.[19] Rietveld refinement indicates that $K_{1.39}Mn_3O_6$ belongs to monoclinic symmetry with a space group of $C12/m1$. The crystal structure of the buckled-layer $K_{1.39}Mn_3O_6$ (BL-KMO) is illustrated in Fig. 2b. X-ray crystallographic analysis shows that Mn ions are classified into two types: Mn(1) and Mn(2). The MnO_6 layer is formed along the *b*-axis through alternating connections of $Mn(1)O_6$ and $Mn(2)O_6$ octahedra, shared along the edges in the *c*-axis direction. From a crystallographic perspective, the charge ordering of Mn^{3+}/Mn^{4+} results in two distinct Mn sites, as Mn^{3+} and Mn^{4+} inhabit different octahedral environments. Since Mn^{3+} is a Jahn–Teller active ion with a larger radius than Mn^{4+}, Mn^{3+} and Mn^{4+} preferentially occupy the Mn(2) and Mn(1) sites,

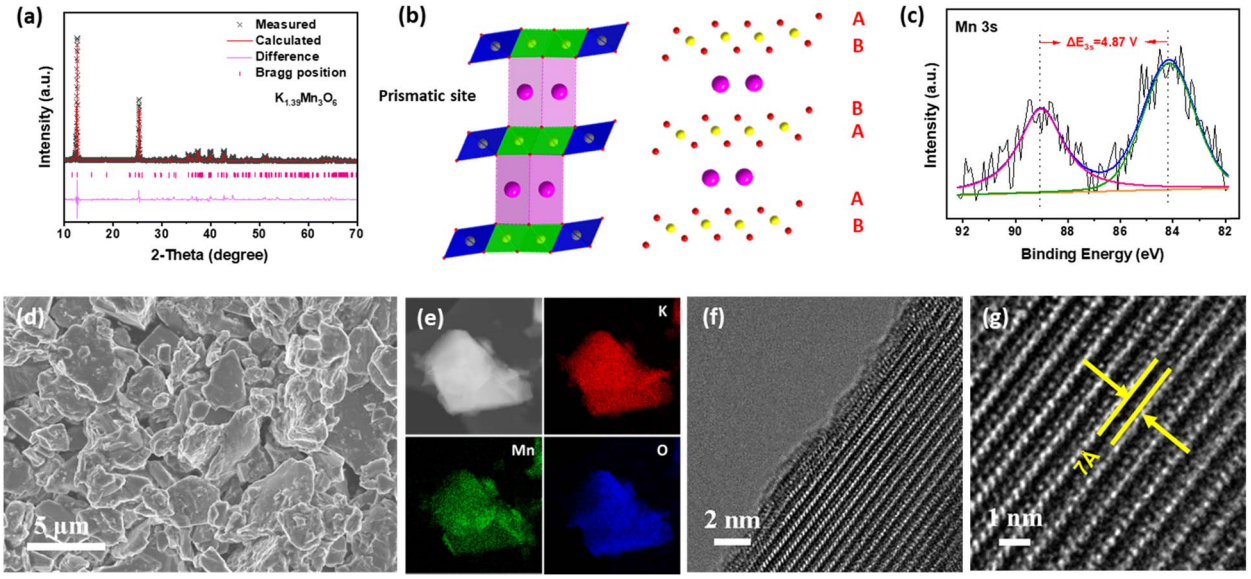

Fig. 2 (a) XRD pattern, (b) crystal structure, (c) high-resolution Mn 3s XPS spectrum, (d) SEM images, (e) STEM image of BL-KMO with corresponding elemental mappings of K, Mn, and O and (f and g) TEM images of buckled-layer $K_{1.39}Mn_3O_6$.

respectively. These findings are consistent with the proposed arrangement of Mn^{3+} and Mn^{4+} in separate rows in birnessite based on extended X-ray absorption fine structure (EXAFS) analysis.[21] Importantly, MO_2 slabs are stacked along the *c*-axis with closely packed oxygen in an ABBA array, while the K ions are accommodated in prismatic sites within the interslab space of the BL-KMO structure. Moreover, all K sites in BL-KMO are crystallographically equivalent, edge-sharing with MnO_6 octahedra on one side and face-sharing with MnO_6 octahedra on the other. In addition to the buckled-layer structure, $K_{1.39}Mn_3O_6$ exhibits characteristics of P2-type oxygen stacking sequences and P3-type K sites in cathodes. The chemical characteristics of BL-KMO were examined through XPS, as depicted in Fig. S4.† The peak of Mn 3s can be deconvoluted into two peaks at 89.02 eV and 84.15 eV (Fig. 2c). The average oxidation state of Mn (V_{Mn}) in BL-KMO can be evaluated from the energy separation (ΔE_{3s}), with V_{Mn} calculated to be 3.52, according to the linear relation: $V_{Mn} = 7.875 - 0.893\Delta E_{3s}$.[22] Correspondingly, the Mn $2p_{1/2}$ and Mn $2p_{3/2}$ peaks in the high-resolution Mn 2p spectrum can be separated into two peaks of Mn^{3+} and Mn^{4+},[23] with approximately equal integral areas (Fig. S5†). The K/Mn atomic ratio was determined to be 0.46 for BL-KMO based on inductively coupled plasma (ICP) measurements, which is very close to the theoretical value. The morphologies and microstructures of BL-KMO were characterized by SEM and HRTEM. As shown in the SEM images (Fig. 2d), the $K_{1.39}Mn_3O_6$ crystal particles exhibit random shapes and sizes. Uniform elemental distributions of K, Mn, and O were observed across the entire particle surface using scanning transmission electron microscopy (STEM) (Fig. 2e). The HRTEM images reveal a highly crystalline structure with interlayer spacings of 7 Å, corresponding to the (201) plane of $K_{1.39}Mn_3O_6$ (Fig. 2f and g).

The electrochemical performance of BL-KMO was evaluated within the voltage range of 2.0–4.2 V (*vs.* K/K^+), using the electrolyte of 2.5 M potassium bis(fluorosulfonyl)imide in triethylphosphate. Cyclic voltammetry (CV) measurements were conducted at a scan rate of 0.1 mV s^{-1}, revealing five distinct redox couples corresponding to the reversible K^+ insertion/extraction coupled with the Mn^{3+}/Mn^{4+} redox reaction (Fig. 3a). Notably, the CV curves show excellent overlap after the first cycle, indicating a good cycling stability. The galvanostatic charge/discharge profiles at a current density of 100 mA g^{-1} are illustrated in Fig. 3b, where the first charge and discharge capacities of BL-KMO were found to be 89.6 mA h g^{-1} and 105 mA h g^{-1}, respectively. After 100 cycles, the capacity retention reached an impressive 91.3%, with average coulombic efficiencies near 99% (Fig. 3c). Furthermore, even at a higher current density of 500 mA g^{-1}, BL-KMO maintained a capacity of 70 mA h g^{-1} after 100 cycles, achieving 99.2% capacity retention (Fig. 3d). A good rate performance was demonstrated by the BL-KMO cathode (Fig. 3e). BL-KMO delivered capacities of 120, 105, 95, 87, 80, 77, 75, 73, 72, 71 and 70 mA h g^{-1} as the current density increased from 50 mA g^{-1} to 100, 150, 200, 300, 400, 500, 600, 700, 800, and 1000 mA g^{-1}, respectively. Importantly, when the current density was reduced back to 50 mA g^{-1}, the capacity recovered to 108 mA h g^{-1}, reaffirming the exceptional performance of the buckled-layer transition metal oxide cathode. The electrochemical impedance spectroscopy (EIS) measurement of the BL-KMO cathode was conducted at the open-circuit voltage state, and the data are presented in Fig. S6.† The semicircle in the high-frequency region corresponds to the charge-transfer resistance (R_{ct}) at the electrode–electrolyte interface, which reflects the electrochemical kinetics. The fitting results reveal that R_{ct} is 1752 Ω.

To further analyze the potassium storage behavior of the BL-KMO cathode, CV measurements were conducted at various sweep rates ranging from 0.1 to 2.1 mV s^{-1} (Fig. S7†). The relationship between peak current (i) and the scanning rate (v)

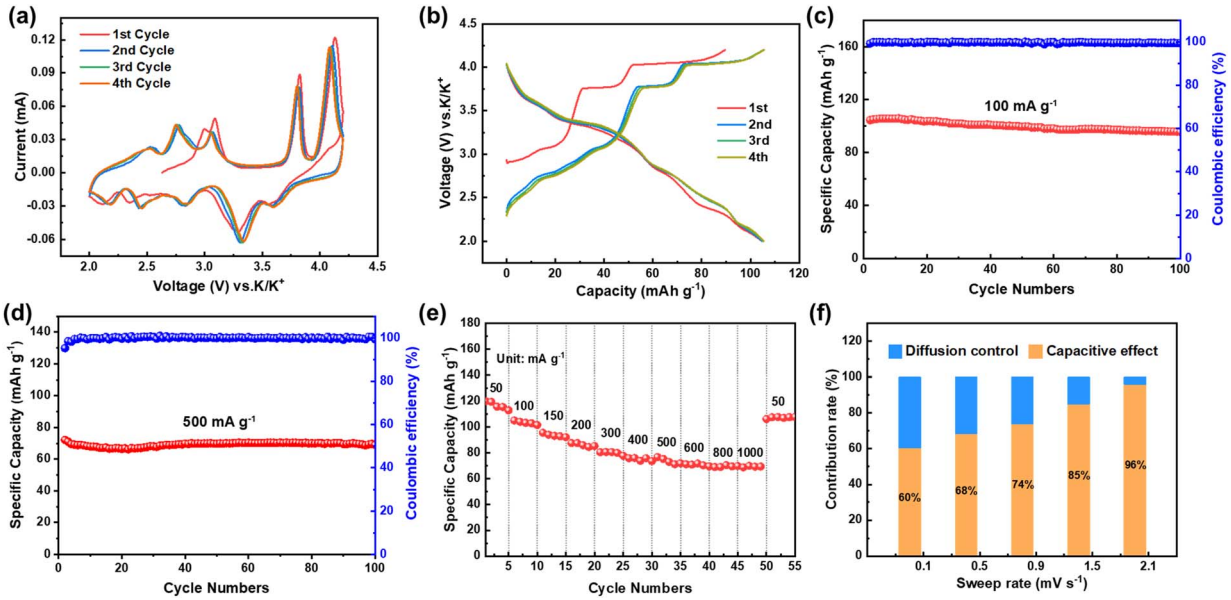

Fig. 3 Buckled-layer $K_{1.39}Mn_3O_6$ cathode, (a) CV profiles at a scan rate of 0.1 mV s^{-1}. (b) Galvanostatic charge–discharge profiles in 1st, 2nd, 3rd and 4th cycles. (c) Cycle performances at a current density of 100 mA g^{-1} for 100 cycles. (d) Cycle performances at a current density of 500 mA g^{-1} for 100 cycles. (e) Rate capability. (f) Normalized capacitive-controlled capacities and diffusion-controlled capacities at different scan rates.

was assessed using a power law model ($i = av^b$), where b is an indicator of the type of charge storage. For BL-KMO, b is approximately 0.6 (Fig. S8†), suggesting a combined mechanism of diffusion and pseudocapacitive processes.[24] The contributions of surface pseudocapacitance and ion intercalation to the overall capacity were quantitatively analyzed. Using the equation $i(V) = k_1v_1 + k_2v^{1/2}$, the charge storage was partitioned into surface capacitive-controlled (k_1v_1) and diffusion-controlled ($k_2v^{1/2}$) processes.[25] The surface capacitive-controlled capacities for BL-KMO at different scan rates are summarized in Fig. 3f.

Ex situ XRD measurements were conducted to investigate the structural evolution and K-storage mechanisms of BL-KMO (Fig. 4a). Two characteristic peaks at (2 0 −1) and (4 0 −2)

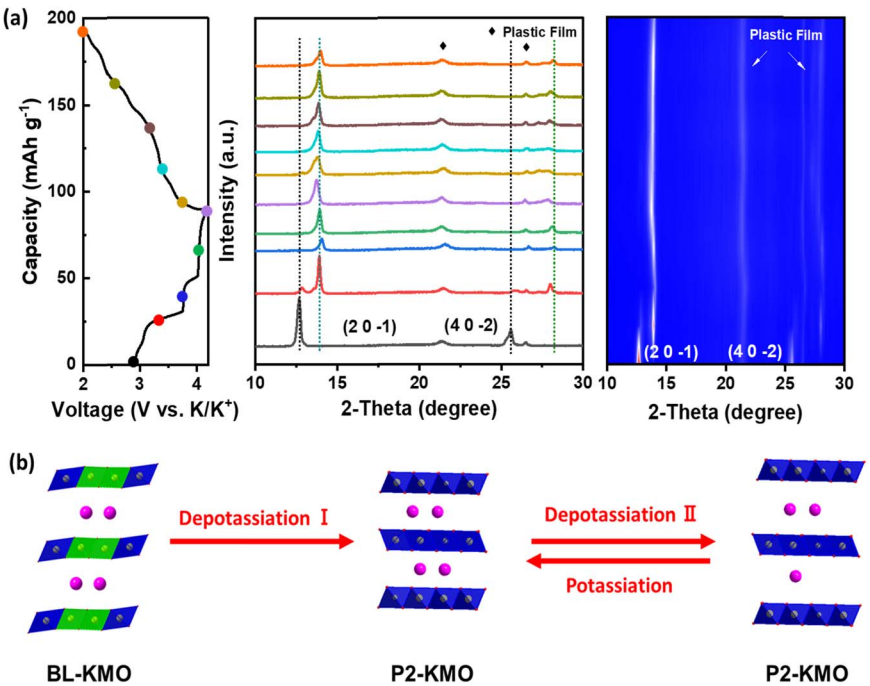

Fig. 4 (a) *Ex situ* XRD patterns at different charge/discharge states at 50 mA g^{-1}. (b) Schematic diagram of the K-ion storage reaction mechanism of the BL-KMO cathode.

respectively located at $2\theta = 12.7°$ and 35.4° were observed. The extraction of K ions can be categorized into two stages: depotassiation I and depotassiation II. During depotassiation I (from open circuit voltage to 3.75 V), both the (2 0 −1) and (4 0 −2) peaks shifted to higher 2θ values with noticeable peak splitting. This suggests a phase transition from the original buckled-layer structure to a P2 structure, while the oxygen stacking (ABBA) remained unchanged throughout the charge/discharge process. As charging progressed from 3.75 V to 4.2 V (depotassiation II), the (2 0 −1) peak at 13.8° gradually shifted towards lower angles, attributed to increased repulsion among the negatively charged MnO_2 slabs. Remarkably, during the discharge process, the peak positions showed little variation, suggesting that although this may represent an intermediate state, the BL-KMO cathode maintained excellent electrochemical performance. A schematic diagram illustrating the K-ion storage reaction mechanism for the BL-KMO cathode is presented in Fig. 4b.

Conclusions

In summary, we leveraged the unique properties of a MOF precursor to successfully synthesize a buckled-layer $K_{1.39}Mn_3O_6$ cathode. The crystal structure analysis results reveal that the charge ordering of Mn^{3+}/Mn^{4+} leads to the formation of two independent Mn sites due to the distinct octahedral environments surrounding Mn^{3+} and Mn^{4+}, forming the buckled-layer structure. Consequently, the buckled-layer $K_{1.39}Mn_3O_6$ cathode exhibits exceptional electrochemical performance. Our findings provide a new design of cathode materials for energy storage.

Data availability

The article and ESI† contain all the experimental and computational data.

Author contributions

Y. X. and A. L. designed the research. A. L. and Z. W. carried out the experiments and analysis. Y. X. revised the manuscript. All authors read and commented on the manuscript.

Conflicts of interest

There are no conflicts to declare.

Acknowledgements

This work was supported by the Fundamental Research Funds for the Central Universities (Grant No. XJ2021007101).

Notes and references

1 X. Zou, P. Xiong, J. Zhao, J. Hu, Z. Liu and Y. Xu, *Phys. Chem. Chem. Phys.*, 2017, **19**, 26495–26506.
2 H. Yang, F. He, F. Liu, Z. Sun, Y. Shao, L. He, Q. Zhang and Y. Yu, *Adv. Mater.*, 2024, **36**, 202306512.
3 J. Zheng, Y. Yang, X. Fan, G. Ji, X. Ji, H. Wang, S. Hou, M. R. Zachariah and C. Wang, *Energy Environ. Sci.*, 2019, **12**, 615–623.
4 L. Sun, G. Li, S. Zhang, S. Liu, J. Yuwono, J. Mao and Z. Guo, *Sci. China: Chem.*, 2024, **67**, 4–12.
5 J. Chen, A. M. Rao, C. Gao, J. Zhou, L. Cha, X. Yuan and B. Lu, *Nano Res.*, 2024, **17**, 9671–9678.
6 Z. Li, L. Ma, K. Han, Y. Ji, J. Xie, L. Pan, J. Li and W. Mai, *Chem. Sci.*, 2023, **14**, 9114–9122.
7 Z. Wang, C. Wei, H. Jiang, Y. Zhang, K. Tian, Y. Li, X. Zhang, S. Xiong, C. Zhang and J. Feng, *Adv. Mater.*, 2023, **36**, 2306015.
8 L. Wu, H. Fu, W. Lyu, L. Cha, A. M. Rao, K. Guo, J. Zhou, S. Wen and B. Lu, *ACS Nano*, 2024, **18**, 13415–13427.
9 L. Wang, S. Zhang, N. Li, J. Chen, Y. Chen, Z. Zhang, L. Tan, X. Niu, Y. Yang, J. Zhang, H. Li, X. Ji and Y. Zhu, *Adv. Funct. Mater.*, 2024, 2408965.
10 Y. Tang, H. Dong, M. Liu, G.-X. Wei, J.-H. Li, W. Tang, Y. Liu, X. Zhu, Y.-H. Feng, Q. Liu, D.-W. Wang, Y. Xiao, P.-F. Wang and B. Xiao, *J. Mater. Chem. A*, 2024, **12**, 14360–14366.
11 Z.-X. Huang, Z.-Y. Gu, Y.-L. Heng, E. H. Ang, H.-B. Geng and X.-L. Wu, *Chem. Eng. J.*, 2023, **452**, 139438.
12 B. Lin, X. Zhu, L. Fang, X. Liu, S. Li, T. Zhai, L. Xue, Q. Guo, J. Xu and H. Xia, *Adv. Mater.*, 2019, **31**, 1900060.
13 K. Sada and P. Barpanda, *Chem. Commun.*, 2020, **56**, 2272–2275.
14 Q. Wu, M. Ren, J. Geng, T. Zhang, F. Li and F. Li, *Fundam. Res.*, 2024, DOI: **10.1016/j.fmre.2024.03.001**.
15 Z. Xiao, J. Meng, F. Xia, J. Wu, F. Liu, X. Zhang, L. Xu, X. Lin and L. Mai, *Energy Environ. Sci.*, 2020, **13**, 3129–3137.
16 H. Chen, X.-W. Gao, Q. Li, R.-Z. Niu, S.-S. Wang, Q.-F. Gu, J.-J. Mu and W.-B. Luo, *J. Mater. Chem. A*, 2024, **12**, 6261–6268.
17 L. Duan, C. Shao, J. Liao, L. Song, Y. Zhang, R. Li, S. Guo, X. Zhou and H. Zhou, *Angew. Chem., Int. Ed.*, 2024, **63**, e202400868.
18 E. Eikeland, N. Lock, M. Filsø, M. Stingaciu, Y. Shen, J. Overgaard and B. B. Iversen, *Inorg. Chem.*, 2014, **53**, 10178–10188.
19 Q. Chu, X. Wang, X. Zhang, Q. Li and X. Liu, *Inorg. Chem.*, 2011, **50**, 2049–2051.
20 A. Li, C. Li, P. Xiong, J. Zhang, D. Geng and Y. Xu, *Chem. Sci.*, 2022, **13**, 7575–7580.
21 V. A. Drits, E. Silvester, A. I. Gorshkov and A. Manceau, *Am. Mineral.*, 1997, **82**, 946–961.
22 R. Dang, N. Li, Y. Yang, K. Wu, Q. Li, Y. L. Lee, X. Liu, Z. Hu and X. Xiao, *J. Power Sources*, 2020, **464**, 228190.
23 X. Hou, C. Li, M. Li, Y. Liu, W. Zhu, Z. Li and Y. Xu, *Chin. J. Chem.*, 2023, **41**, 2597–2603.
24 V. Augustyn, J. Come, M. A. Lowe, J. W. Kim, P.-L. Taberna, S. H. Tolbert, H. D. Abruña, P. Simon and B. Dunn, *Nat. Mater.*, 2013, **12**, 518–522.
25 N. Wu, Z. Zhao, R. Hua, X. Wang, Y. Zhang, J. Li, G. Liu, D. Guo, G. Sun, X. Liu and J. Zhang, *Adv. Energy Mater.*, 2024, **14**, 2400371.